Investigating the Excitation Spectrum of ^{8}He from Inelastic Scattering with Deuterons

by

Colby O'Keefe

A THESIS SUBMITTED IN PARTIAL FULFILMENT OF
THE REQUIREMENTS FOR THE DEGREE OF

BACHELOR OF SCIENCE

in

Honours Physics

(Department of Astronomy and Physics, Dr. Rituparna Kanungo supervising faculty)

.....

.....

.....

.....

.....

SAINT MARY'S UNIVERSITY

April 26, 2022

Abstract

Investigating the Excitation Spectrum of ^{8}He from Inelastic Scattering with Deuterons

by *Colby O'Keefe*

submitted on April 26, 2022:

Rare isotopes are nuclei with very short half-lives and can have a large asymmetry of neutrons to protons. These isotopes can have unusual structures such as halos that can exhibit a phenomenon known as a Soft Dipole Resonance (SDR). One rare isotope of interest is 8-Helium (^{8}He) which is the most neutron-rich bound nucleus currently known, with a neutron to proton ratio of 3. In previous investigations of ^{8}He two excited states (2^{+} and 1^{+}) were observed with drastically conflicting reports on their locations. The inconsistent reports on the 2^{+} state, in particular, have been postulated to be due to the excited state being mixed with a low-lying SDR state. Through an experiment conducted at the IRIS facility located at TRIUMF, Canada's particle acceleration center, the excited spectrum of ^{8}He has been investigated. The goal of this study is to get additional measurements on the excited states of ^{8}He as well as explore the possibility of the 2^{+} state being mixed with a SDR. In this thesis, I will outline the experimental set up and the data analysis to determine the Q-value spectrum of ^{8}He from the ^{8}He(d,d$'$)^{8}He* reaction.

Acknowledgment

I would like to express my gratitude to my academic supervisor Dr. Rituparna Kanungo for her guidance throughout this project. I also want to thank Dr. Greg Christian for agreeing to act as a second reader for my thesis. I want to thank the IRIS collaboration for sharing their knowledge and insight throughout this project. I also want to thank my family for their support and aid with proofreading. Finally, I want to thank the Canadian Institute of Nuclear Physics (CINP), NSERC, TRIUMF, and Saint Mary's University.

Contents

List of Figures

Chapter 1

INTRODUCTION

1.1 EXOTIC NUCLEI

The building blocks of the universe as we know it are protons, neutrons, and electrons. Everything that we interact with from the air we breathe to the breakfast that you ate this morning is comprised of atoms. Atoms can further be broken down into a group of protons and neutrons surrounded by electrons. But this begs some very important questions such as, why do different materials vary so drastically in appearances and properties if they are made of the same three particles? How are protons, neutrons, and electrons formed into atoms? To answer the latter, two ingredients are necessary to form an element and they are matter and energy. These two components, needed to form an element, are one of the reasons why most elements are created via stellar processes. Elements lighter than iron are thought to have formed in stars by nuclear fusion. Elements heavier than iron are thought to be produced by supernovas and neutron star mergers where there is a surplus of energy that allows for β^- decay and proton/neutron capture to occur [9].

Nuclei are a combination of neutrons and protons. A nucleus can be characterized by its proton number Z, its neutron number N, and its mass number A $(Z+N)$. The proton number of a nucleus determines the element, and two nuclei that share the

same number of protons but has a different number of neutrons are called isotopes. Many elements we encounter in our day-to-day lives have nuclei that are in a stable arrangement of protons and neutrons. Stable nuclei tend to have a similar number of protons and neutrons. However, most elements that exist are not stable which means they undergo radioactive decay and hence have a life span dictated by their half-life. Isotopes that are not stable are called rare isotopes. Nuclei with very short half-lives whose properties are exhibiting marked deviations from our known knowledge are called exotic nuclei.

This thesis is concerned with the exotic nucleus ^{8}He. ^{8}He is a neutron-rich nucleus which means the nucleus has more neutrons than protons. ^{8}He lies on what is known as the neutron drip-line, where any isotope of He with a larger neutron number than ^{8}He decays by the emission of a neutron. Figure 1.1 shows the nuclear landscape near ^{8}He. Studying the structure of ^{8}He will shed light on the properties and structures of the drip-line nuclei.

1.2 Nuclear Shell Model

Very similar to how electrons occupy orbitals around the nucleus, nucleons (neutrons and protons) occupy orbitals within the nucleus. Because of the strong nuclear interaction between nucleons, the protons and neutrons sit in a potential within the nucleus. This potential cannot be expressed analytically, but an approximation com-

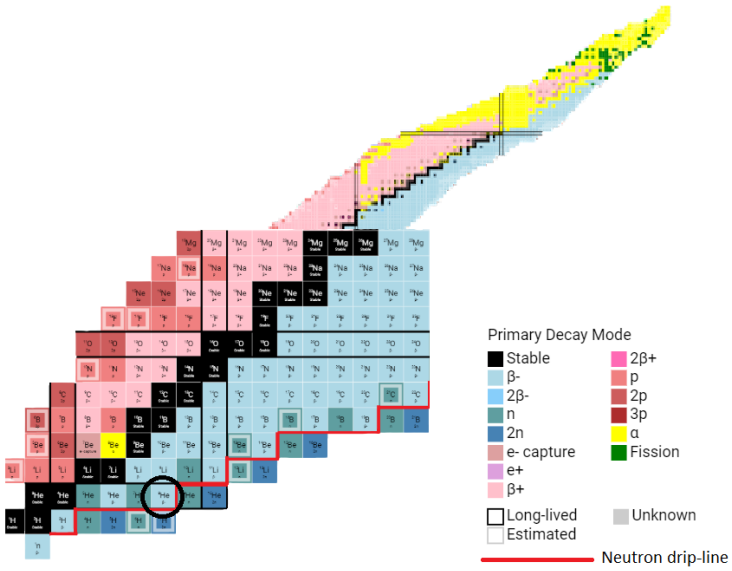

Figure 1.1: The nuclear landscape of nuclei around ^{8}He. The black circle shows ^{8}He and the red line shows the neutron drip-line [12].

monly used is the Woods-Saxon potential which is as follows,

$$V(r) = \frac{-V_0}{1 + e^{\frac{r-R}{a}}} \tag{1.1}$$

where R is the radius of the nucleus, a is the diffuseness, V_0 is the depth of the potential well, and r is the distance from the nucleus center [9].

The orbitals of the nucleus are filled separately for neutrons and protons according to the Pauli exclusion principle. Taking into account spin-orbit coupling, all energy levels not spherically symmetric will split with the new angular momentum given as follows,

$$j = l \pm \frac{1}{2} \tag{1.2}$$

where l is the orbital angular momentum and j is the total angular momentum. It

follows that each state will have a degeneracy given by the following,

$$degeneracy = 2j + 1 \tag{1.3}$$

this means that each energy level can hold $2j + 1$ protons and neutrons. Figure 1.2 shows the first few nuclear energy levels. The large gaps between levels occur when the proton or neutron number is at what is known as a magic number. These magic numbers correspond to the number of nucleons needed to fill a shell, hence a large amount of energy will be needed to move a nucleon to the next energy level [9].

The ground state of a nucleus is the lowest energy arrangement of nucleons. In the context of the shell model, the ground state is typically where nucleons are placed from the lowest energy level upwards. When at least one nucleon occupies a higher orbital than the ground state the nucleus is said to be in an excited state. An excited state can be classified by its angular momentum and parity quantum numbers usually reported in the form J^{π} where J is the total angular momentum and π is the parity. There are many different methods that can excite a nucleus which includes adding energy to a nucleon or collective excitation (e.g. vibration or rotation of the nucleons). The excitation energy is the amount of energy required for a nucleon to be placed in a higher energy level than in the ground state [9].

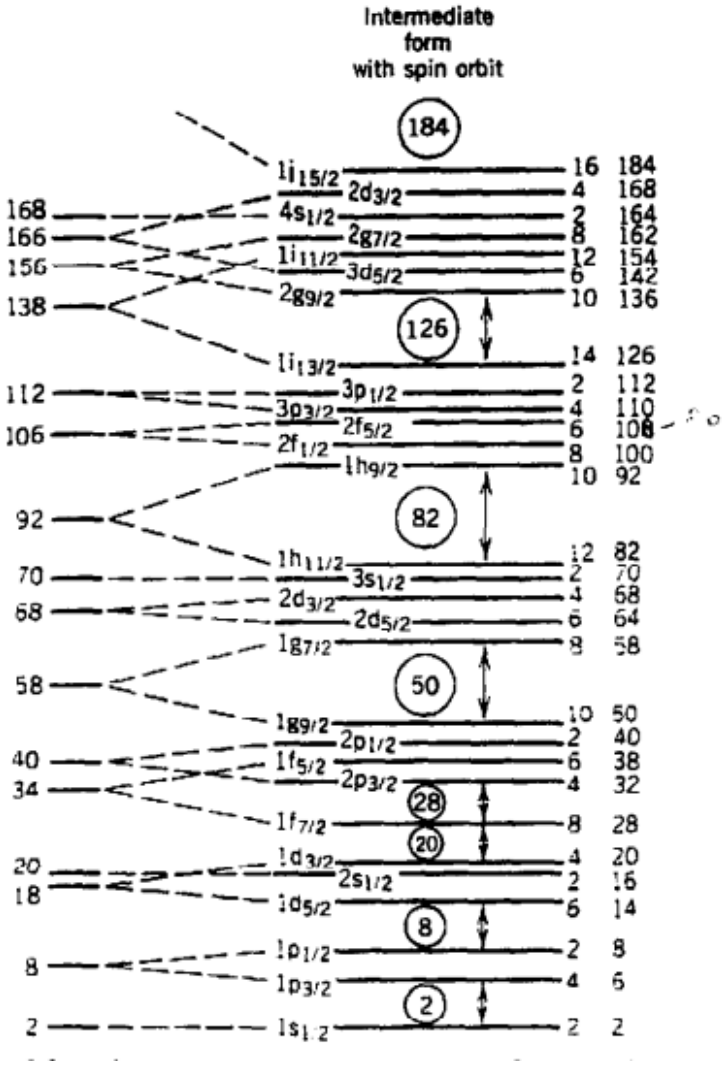

Figure 1.2: Low-lying energy levels of a nucleus with spin-orbit splitting [9].

1.3 ^{8}He Excited States

There have been many theoretical and experimental studies investigating the low-lying excited spectrum of the ^{8}He nucleus. The two excited states commonly observed in the literature have a spin-parity of 2^{+} and 1^{+}. Theoretical calculations using Monte Carlo methods place the 2^{+} state around 2.5-2.8 MeV and the 1^{+} state around 3.2-4.4 MeV [11]. More recent calculations on the 2^{+} excited state location give results closer to the 3.2-3.5 MeV range [6]. On top of theoretical studies, there have been a number

of experimental studies looking at the excitation spectrum of ^{8}He.

Golovkov et al. was studying the low-lying spectrum of ^{8}He from the ^{3}H(^{6}He,p)^{8}He transfer reaction using a tritium gas target. This study was conducted at JINR and used a primary beam of ^{11}B ions at 34 MeV/u with secondary beams of ^{8}He and ^{6}He. The excited spectrum was found by using the missing mass technique which will be discussed in Chapter 3.7. This study observed a 2^{+} and 1^{+} state at 3.57 $\pm$ 0.12 MeV and $\sim$5.4 MeV respectively. There was also a third possible excited state observed at $\sim$7.5 MeV but the possible nature of this resonance was not discussed [4].

Another study by J. Xiao et al. at RIKEN was investigating the breakup reaction of ^{8}He on two different targets made of C and CH_2. The study used a primary beam of ^{13}C at 155 MeV/u and a secondary beam of ^{8}He at 82.3 MeV/u. This study observed a 2^{+} state at 2.99 $\pm$ 0.02 MeV and a unknown state at 4.14 $\pm$ 0.06 MeV [13].

Additionally, Karin Markenroth Bloch et al. was looking at the breakup reaction of ^{8}He in a carbon target at GSI. The primary beam was ^{18}O at 340 MeV/u with secondary beams of ^{6}He and ^{8}He at 240 MeV/u and 227 MeV/u respectively. This study used the invariant mass method to reconstruct the relative energy spectra. The study then used a Monte Carlo simulation to fit two Breit–Wigner shaped resonances to the data and found a overlap of a narrow 2^{+} state at 2.9 $\pm$ 0.2 MeV and a broad state at 4.15 $\pm$ 0.20 MeV [10].

The measurements for the excited states in these studies vary drastically from one another. The first excited state varies from around 2.9-3.6 MeV in the previously mentioned studies. This state has a spin-parity of 2^{+} which is known from previous measurements of the differential cross-sections of the resonance [10]. The second

resonance also seems to have a large discrepancy associated with it, with some sources reporting it to occur as low as 4 MeV and others as high as 5.4 MeV [10]. The spin-parity of this second resonance is not yet known but it is assumed to be 1^+ based on theoretical predictions. The cause for this large discrepancy in the measured locations of the ^{8}He excited states are not yet known; however there have been some theoretical predictions that suggest the 2^+ state could be mixed with a Soft Dipole Mode (1^- continuum) [5].

1.4 Soft Dipole Mode

A Soft Dipole Mode (SDM) is when the halo nucleons oscillate against the core of the nucleus. ^{8}He is thought to be a five-body system with an alpha particle (^4He) core and a four-neutron halo [6]. Figure 1.3 shows a diagram of a SDM in ^{8}He.

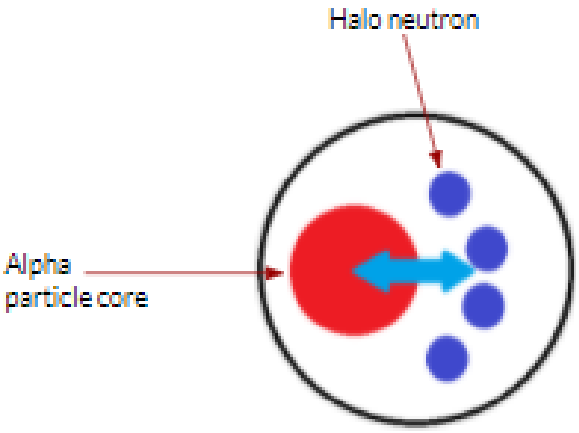

Figure 1.3: Soft Dipole Mode illustration in ^{8}He.

Karin Markenroth Bloch et al was studying the breakup reaction of ^{8}He in a carbon target and measured the angular distribution for the full excitation spectrum

measured (0-6 MeV). The study calculated the angular distribution for a dipole and quadrupole transition using the distorted wave Born approximation (DWBA). The measured angular distribution was compared to the calculated angular distributions. Evidence was found to support the presence of a strong dipole mode in the excitation spectrum of ^{8}He. The measured angular distribution indicated that the board state observed at 4.15 MeV could have a spin-parity of 1^{-} [10].

Another study conducted at the IRIS facility located at TRIUMF studied the inelastic scattering of ^{8}He with a solid hydrogen target. The study made measurements of the angular distribution around the observed 2^{+} resonance state. The study then calculated the angular distribution for a dipole and quadrupole transition using the DWBA [6]. Figure 1.4 shows the measured angular distribution, and the calculated curves for the dipole transition (the solid/dotted green lines), and quadrupole transition (the blue dashed/red solid lines). This study didn't observe any evidence of a SDM in the angular distribution [6].

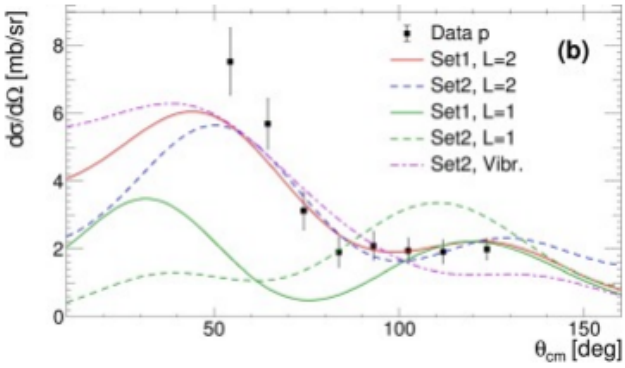

Figure 1.4: The angular distribution of the 2^{+} excited state in ^{8}He. The dots are the measurements of the angular distribution while the curves are the calculated angular distribution using different models [6].

The study conducted at the IRIS didn't find any evidence of a dipole resonance

near the 2^+ state as predicted by Karin Markenroth Bloch et al. To figure out where to go from here it is necessary to look at another nucleus ^{11}Li. A study that was also conducted at the IRIS facility was investigating the inelastic scattering of ^{11}Li with a solid deuterium target. This study was able to observe a SDM for an excited state near 1.03 MeV by comparing the measured angular distribution to the calculated curve from a DWBA calculation for a dipole transition [8]. The dipole resonance observed in this study was a special type of dipole resonance known as an isoscalar dipole resonance. Since deuterium has isospin of 0 it is known as an isoscalar probe, hence, the only type of dipole excitation is isoscalar in nature [8]. A logical next step to determine if there is a low-lying SDM in ^{8}He near the 2^+ state is to try and excite an isoscalar dipole resonance with inelastic scattering using an isoscalar probe.

1.5 Nuclear Reactions

Before the experimental setup is discussed, methods for studying the structure of exotic nuclei should be noted. One such method used for centuries to study the properties of exotic nuclei is using nuclear reactions. Many of the studies looking at the excited spectrum of ^{8}He mentioned in the previous two sections used a variety of different types of nuclear reactions to study the nucleus' structure. ^{8}He and other exotic nuclei have very short half-lives, as such, they cannot be used as stationary targets. Instead, reactions to study exotic nuclei typically involve the nuclei of interest being created in the form of a beam produced by an accelerator using a fragmentation reaction. The target for reactions used to study exotic nuclei is typically a light stable

element.

The reaction between the heavier beam-like nuclei (A) and the lighter target element (b) is written in the following form,

$$A + b \rightarrow C + d \tag{1.4}$$

with the heavier product being denoted C and the lighter product being denoted d. The first reaction of interest when studying exotic nuclei is scattering reactions. There are two types of scattering events that can occur, elastic and inelastic scattering. In a scattering reaction, the product nuclei are the same as the reactants. In the elastic case, kinetic energy is conserved, and the reaction has the following form,

$$A + b \rightarrow A + b \tag{1.5}$$

In the inelastic case, kinetic energy is not conserved because at least one product is put into an excited state. Inelastic scattering has the following form,

$$A + b \rightarrow A^{*} + b^{'} \tag{1.6}$$

The second reaction of interest when studying rare isotopes is transfer reactions. A transfer reaction is where nucleons are transferred between the reactants. This type of reaction has the same form as Equation 1.4.

In this experiment, a ^{8}He beam reacted with a solid deuterium target. The scattering reaction between ^{8}He and deuterium was studied where both elastic scattering

and inelastic scattering events occurred.

Chapter 2

Experimental Overview

The experimental data were collected at the IRIS facility located at TRIUMF, Canada's particle accelerator center, in Vancouver, BC. One reason why TRIUMF is at the frontier of subatomic physics research is that it is home to the world's largest cyclotron which can produce protons up to 500 MeV [6]. These high-energy protons are what allow researchers to produce and study rare isotopes that have very short half-lives and would naturally only be found in extreme environments in the universe. This chapter will discuss the experimental setup at IRIS.

2.1 Radioactive Ion Beam Production

The radioactive isotope beam (RIB) is produced at TRIUMF using a method known as isotope separation on-line (ISOL). ISOL works by colliding a primary beam with a target which causes the beam to break into a variety of radioactive nuclei via fragmentation and fission reactions. In this experiment, the ^{8}He beam was produced by colliding a 500 MeV proton beam from TRIUMF's cyclotron with a SiC target. The resulting ^{8}He beam was re-accelerated to 8.35 AMeV and then sent to ISAC rare-isotope reaction spectroscopy station (IRIS) where the experiment was performed [6].

2.2 IRIS FACILITY

The IRIS facility is located at TRIUMF's Isotope Separator and Accelerator (ISAC-II) facility and is designed to study one and two-nucleon transfer reactions as well as elastic and inelastic scattering between exotic nuclei and a stable nucleus. The primary reaction of interest at IRIS involves isotopes of hydrogen as the target is typically made of H_2 or D_2. Figure 2.1 shows the components and layout of the IRIS facility. The RIB first enters the Ionization Chamber (IC), then the beam reacts with the solid H_2/D_2 target. After the beam reacts with the target the scattered particles and unreacted beam gets picked up by several charged particle detectors which consist of both silicon detectors and scintillators [7].

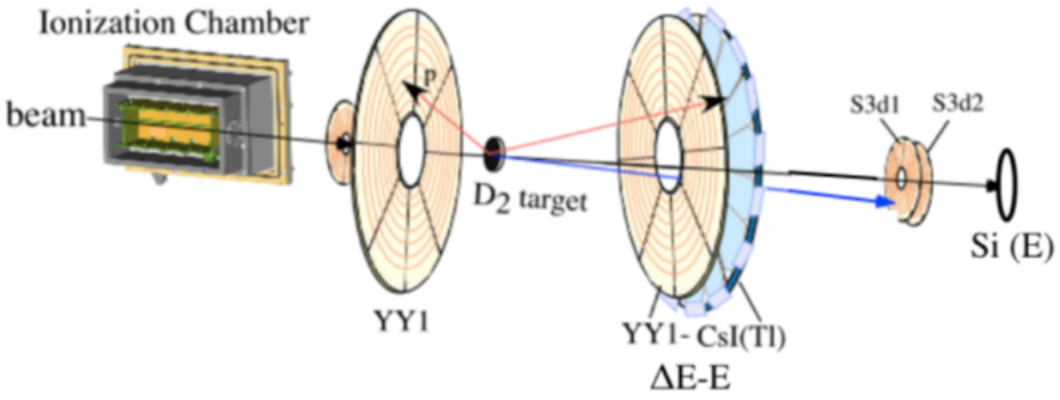

Figure 2.1: Layout of the IRIS experimental setup.

2.2.1 IONIZATION CHAMBER

The first device the incoming RIB comes into contact with when it enters IRIS is the Ionization Chamber. The IC is used for identifying any contaminants in the RIB.

The IC is a gas-filled detector located upstream of the target. The detector is filled with Isobutane (C_4H_{10}) gas kept at a pressure of 19.5 torr and has two SiN_2 windows. Figure 2.2 shows the schematic for the IC. Once the RIB reaches the IC the beam first passes through a 40 nm SiN_2 window and then passes through 229 mm of the gas while depositing some of its energy by ionization. Within the IC there is a negatively charged field cage that drifts the electrons released by the ionization process towards a series of anode pads. The charge collected then creates a voltage signal which is read by the data acquisition system (DAQ). Finally, the beam leaves the IC through a second 50 nm SiN_2 window where it proceeds to the scattering chamber.

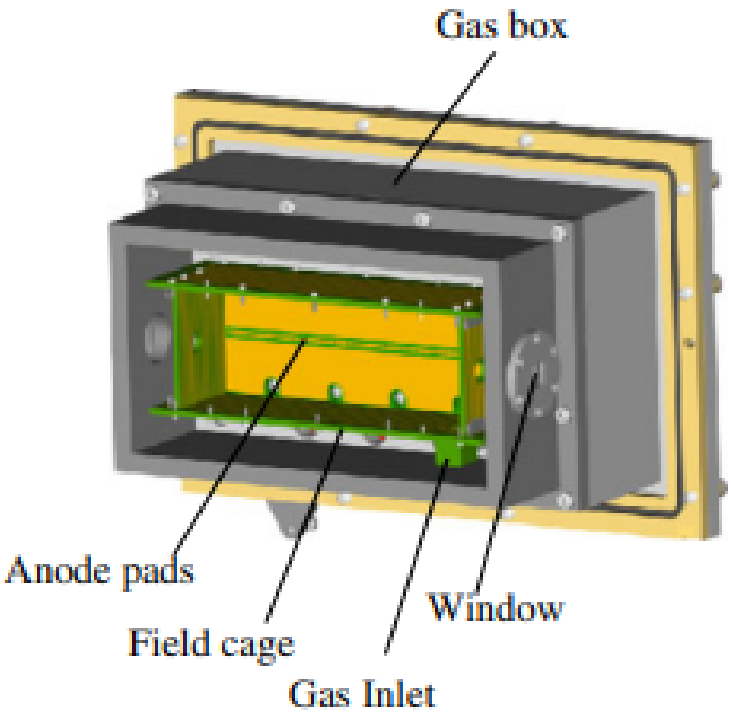

Figure 2.2: Ionization Chamber schematic [7].

2.2.2 The Solid H_2/D_2 Target

Once the RIB leaves the IC and enters the scattering chamber the beam encounters the target. The H_2/D_2 target is the most innovative feature at IRIS, this is because the density of the H_2/D_2 target maximizes the number of interactions between the target and rare isotope of interest. The target is surrounded by a heat shield made of copper. Within the heat shield, there is a thin sheet of silver (Ag) foil with a thickness of 4.3 μm. The Ag foil is placed on the copper cell which cools the foil to about 4K. In the target cell, there is a nozzle called a diffuser which sprays deuterium/hydrogen gas onto the Ag foil freezing it. The diffuser is connected to an actuator which allows the diffuser to be moved in place to create the target and then moved out of the path of the beam after forming the target. The targets created at IRIS are typically around 50 μm or 100 μm in thickness. In this experiment the target created was D_2 with a thickness of approximately 50 μm. Figure 2.3 shows a picture of the target cell and its components.

For this experiment, the target was placed in a manner where the Ag foil was facing upstream. As such the beam will lose energy through the Ag foil before the reaction occurs at the D_2 target.

2.2.3 Charged Particle Detectors

After the RIB reacts with the target the incoming nuclei get picked up by several different charged particle detectors. Upstream of the target there are two silicon detectors, an S3 detector, and a YY1 detector. Downstream of the target there is an-

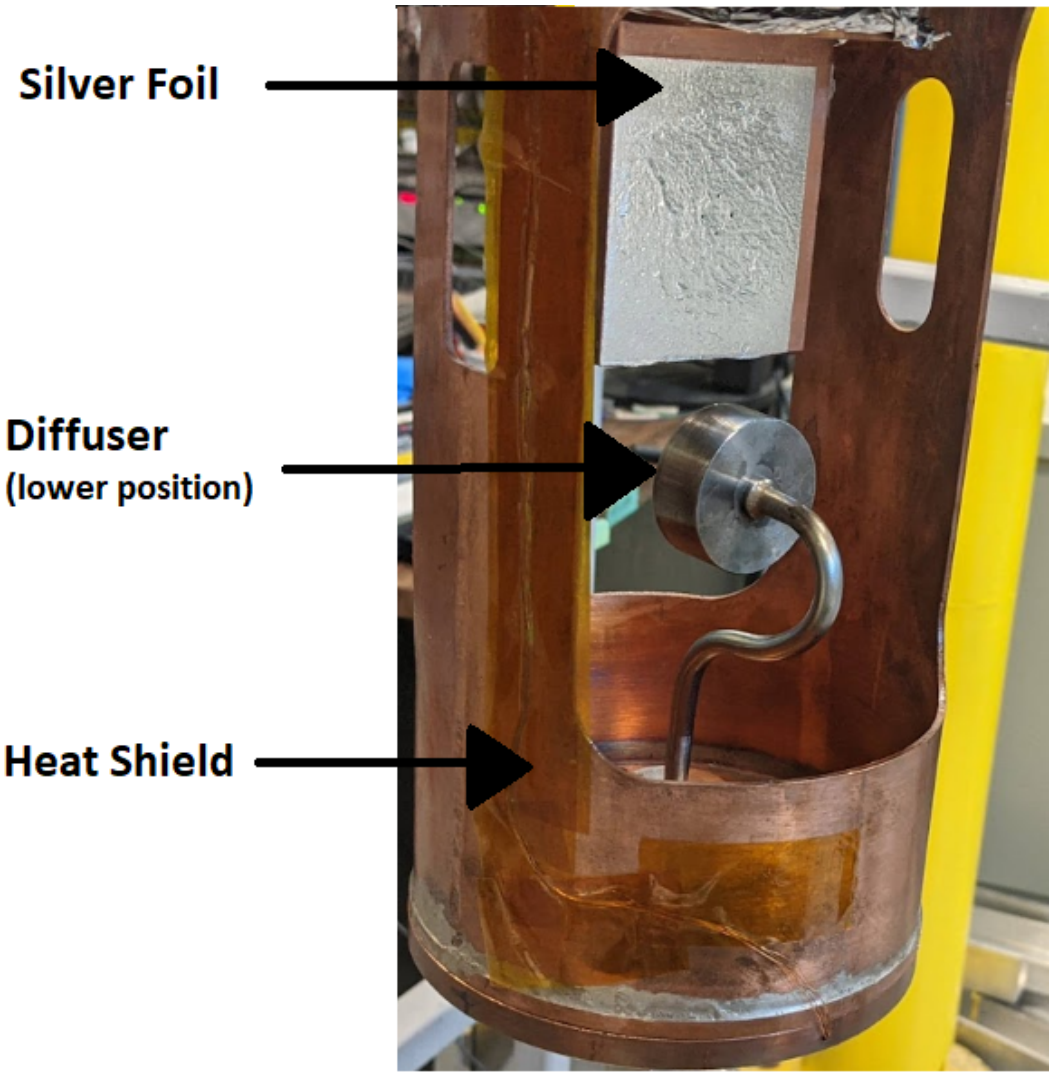

Figure 2.3: The solid H_2/D_2 target.

other YY1 detector, CsI(TI) scintillator, two downstream S3 detectors, a scintillator, and a silicon surface barrier (SSB) detector. The layout of these detectors is shown in Figure 2.1.

The YY1 detector is a segmented silicon strip detector that consists of eight azimuthal sectors, where each sector is divided into 16 strips called rings that give different polar angles. Figure 2.4 shows a diagram of a YY1 sector. Each detector segment reads the energy deposited by any incident particle. The rings of the detector

allow for the scattering angle of the incident particle to be determined. The upstream YY1 detector covers the scattering angles of $\theta_{lab} = 124^\circ$ - 151° and the downstream detector covers the angles of $\theta_{lab} = 11^\circ$ - 28°.

The CsI(TI) detector is placed directly behind the downstream YY1 detector. CsI(TI) detector is divided into 16 sectors without any angular regions. Since the CsI(TI) is positioned directly behind the YY1 detector, the scattering angle of the incident particle can be resolved from the YY1 detector assuming the particle is incident on both detectors. The purpose of the YY1 and CsI(TI) detector is to measure the energy and scattering angle of light particles such as protons and deuterons. The YY1 and CsI(TI) detectors create what is known as a ΔE-E telescope where the light particles lose some of their energy passing through the YY1 detector and deposit their remaining energy in the CsI(TI) detector. This allows for the scattered light particles to be identified based on the amounts of energy deposited in the CsI(TI) and YY1 detectors. This process will be described in more detail in Chapter 3.6.

The S3 detectors are double-sided with one side being segmented into 24 rings and the other into 32 sectors. The ring side of the S3 detector is shown in Figure 2.4. The S3 detector works similarly to the YY1 detector. The upstream S3 detector covers the scattering angles of $\theta_{lab} = 166^\circ$ - 176° and the downstream detector cover the angles of $\theta_{lab} = 2^\circ$ - 7°. The goal of the S3 detectors is to measure the energy and scattering angles of heavy beam-like nuclei.

Finally, the scintillator and SSB detect any unreacted beam. All of these detectors together allow us to measure all light and heavy products from the beams' interaction with the target. In the current experiment, the upstream detectors and SSB were

not used in the data analysis. Only the S3, YY1, and CsI(TI) downstream detectors were used in the data analysis to generate the Q-value spectrum.

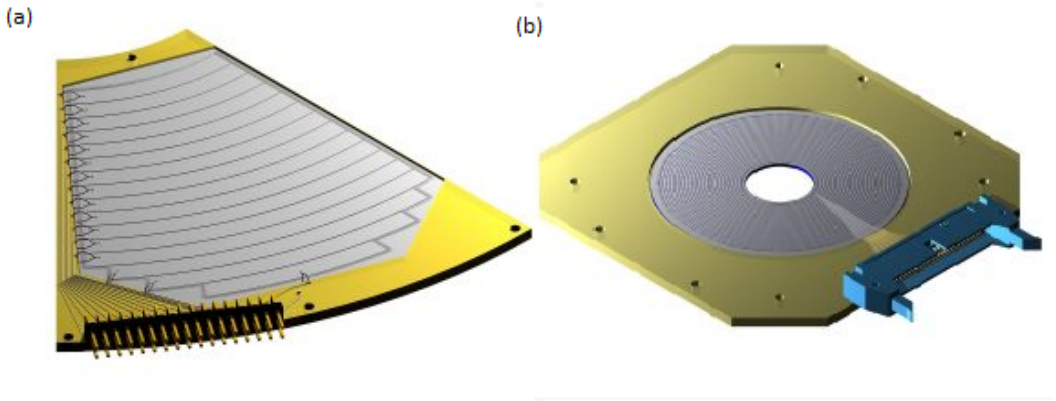

Figure 2.4: (a) Shows a sector of the YY1 detectors [1] and (b) shows the ring side for the S3 detector [2].

Chapter 3

Experimental Analysis

To generate the excitation spectrum and uncover the excited state of the ^{8}He nucleus the various detectors described in the previous section must be calibrated. This chapter describes the process used to calibrate the detectors and how the calibrated data was used to determine the Q-value spectrum.

3.1 Identification of Beam Species

The first step in analyzing the data is to identify the particle species in the RIB and isolate the isotopes of interest which in this experiment is ^{8}He. The various beam species can be distinguished from one another based on the energy loss measured within the IC. The purpose of the IC is to provide information on the atomic number of particles present in the RIB. The energy a particle loses through the IC is dependent on the stopping power of the charged particle through matter. The stopping power describes how much energy a particle will lose through some unit length of a material and is mathematically defined as follows,

$$-\frac{\mathrm{d}E}{\mathrm{d}x} \propto \frac{Z^2}{v^2} \tag{3.1}$$

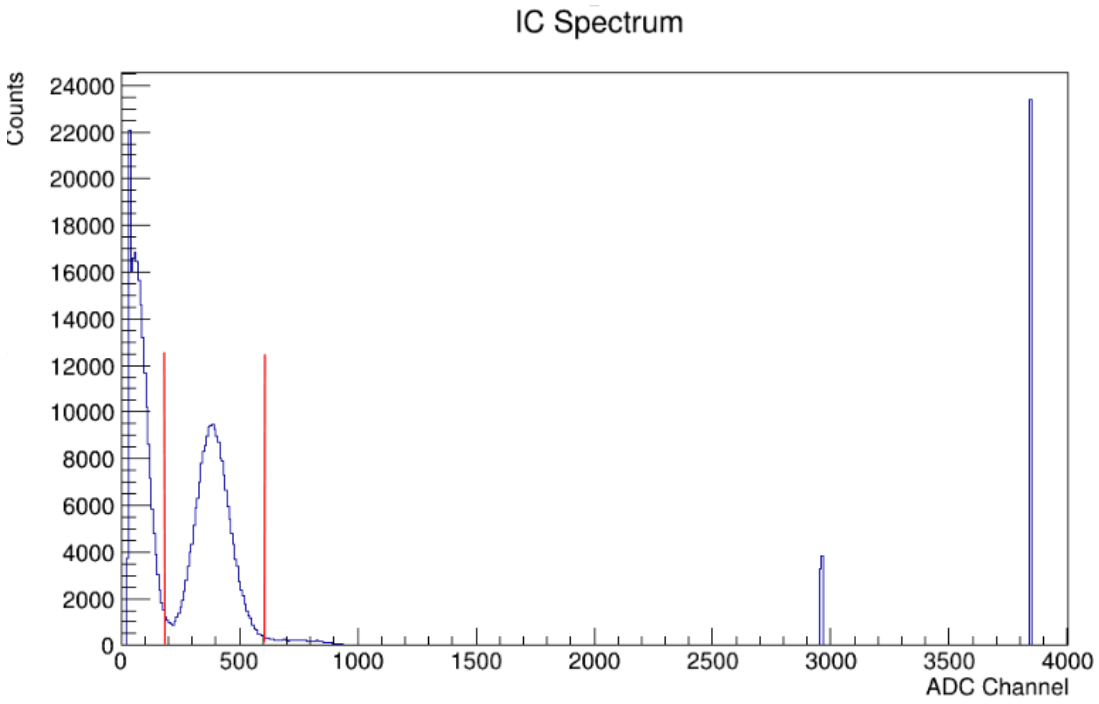

Figure 3.1: ADC spectrum of the Ionization Chamber with a gate placed around the ^{8}He peak represented with vertical red lines

where v is the velocity and Z is the atomic number of the charged particle. The Z^2 dependence allows us to differentiate particles of different atomic numbers. Figure 3.1 shows the ADC spectrum measured by the IC. In the spectrum, only a single gaussian peak was observed meaning the ^{8}He beam was pure i.e. no contaminants were present besides some background noise. Despite the beam being pure, a gate was placed around the ^{8}He peak represented by the red vertical lines in Figure 3.1. The analysis forward will constrain the data to only events originating from within this gate.

3.2 Detector Calibration

When a charged particle hits the detector it transfers a portion or all of its energy to that detector. The deposited energy then generates an analog signal which is digitized by a 12-bit Analog-to-Digital Converter (ADC). The ADC classifies the signal into 4096 channels based on the signal's peak voltage. The goal of a calibration is to convert the measured channel number into a physically meaningful quantity such as energy. The relationship between the ADC channel and energy in MeV is given by the linear equation below,

$$E = g \times (c - p) \tag{3.2}$$

where E is the deposited energy in MeV, g is the gain in MeV/channel i.e. a scaling factor between ADC channel and energy in MeV, c is the peak ADC channel, and p is the pedestal i.e. the zero energy channel in the ADC spectrum or in other words the channel where the energy is zero. The general process to calibrate a detector is to determine the gain and pedestal values for each segment of a given detector. In the proceeding sections the calibration method used for the S3, YY1 and CsI(TI) detectors are described.

3.3 Downstream S3 Detectors

This section will discuss the calibration of the S3 detectors. The S3 calibrations were done using experimental data obtained from the elastic scattering of ^{8}He with the Ag foil i.e. data collected without the D_2 target. The S3 detectors work as a ΔE-E

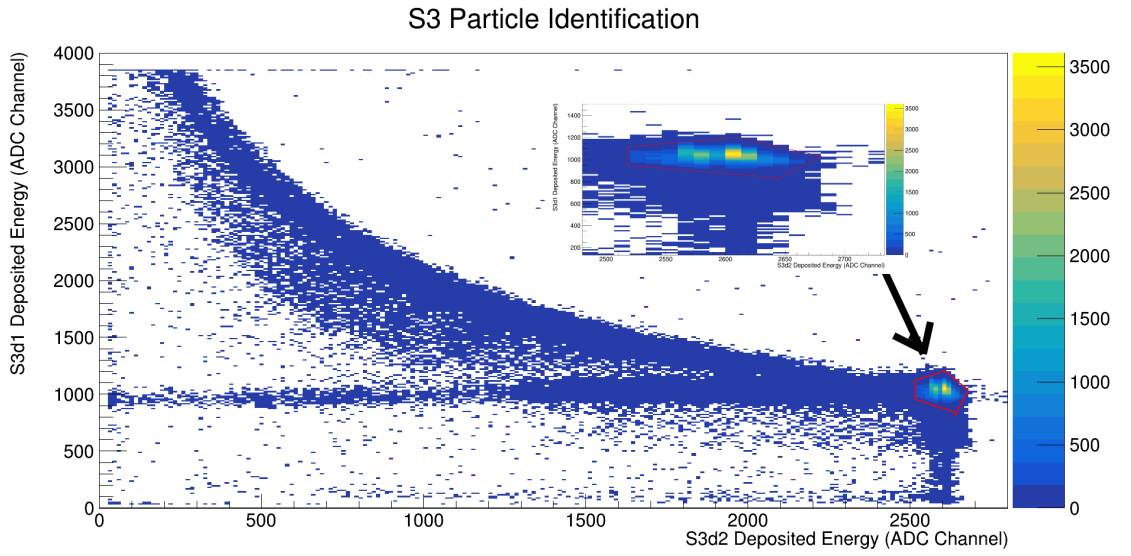

Figure 3.2: The ΔE-E telescope for the S3 detector. The red polygon is the gate for the elastically scattered ^{8}He events.

telescope much like the YY1-CsI(TI) detectors where the scattered ^{8}He first deposited part of its energy into the S3d1 detector while the remaining energy is deposited into the S3d2 detector. The telescope can be used to select the elastic events and then this data can be used to calibrate. Figure 3.2 shows the energy deposited in S3d1 vs. S3d2 detector and the red polygon shows the gate used to select the elastic events. As mentioned in the previous chapter the S3 detectors are double-sided with one side consisting of rings and the backside with sectors. It was decided that only the ring side of the detector was to be calibrated hence the goal is to find a gain and pedestal value for each ring of the two detectors. Using the elastic gate, the ADC spectrum for each ring showed a peak and this peak was then fitted using a gaussian. Figure 3.3 shows the ADC peak and the fitted gaussian. The mean of the fitted gaussian gave the channel number corresponding to the peak position. The energy corresponding to the peak was found using kinematic calculations taking into account the energy loss

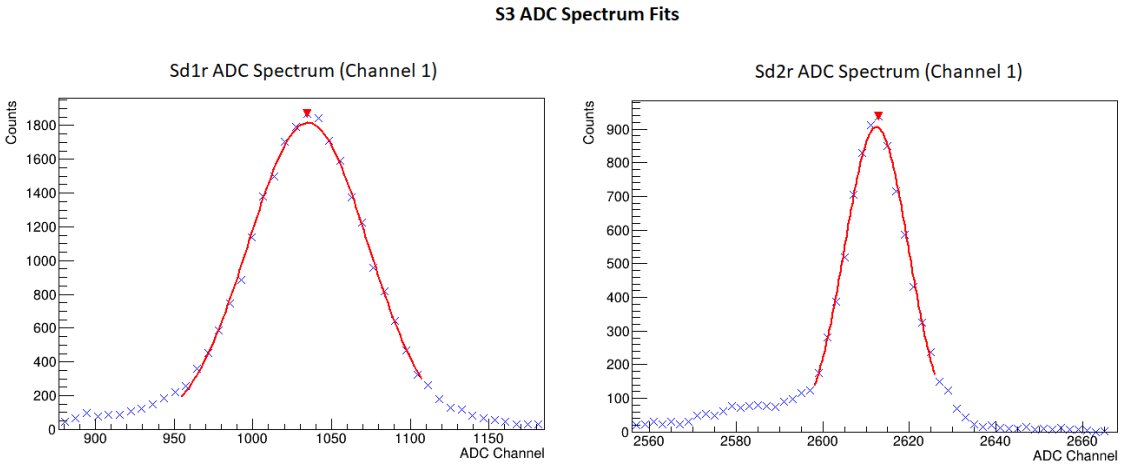

Figure 3.3: The elastic ADC spectrum for the S3 detectors fitted with a gaussian.

before the scattering event. The scattering point was assumed to be the middle of the Ag foil thickness because this is the average point where the scattering event will occur. The energy the scattered particle lost in the dead layers of the S3 detectors was also taken into account. Dead layers are regions in the detector where the particle loses energy but it is not recorded.

Next, the pedestals were found using data that the detectors collected without a beam present. The peak of the ADC spectrum for each ring was once again fitted with a gaussian and the mean of that gaussian was taken as the pedestal value. Figure 3.4 shows the peak for the pedestal data. To complete the calibration the gain can be found by rearranging equation 3.2 to get the following,

$$g = \frac{E}{c - p} \tag{3.3}$$

The calibrated energy vs. scattering angle for the elastic scattered ^{8}He with the Ag foil was plotted in Figure 3.5. The calibrated S3 detectors can now be used to

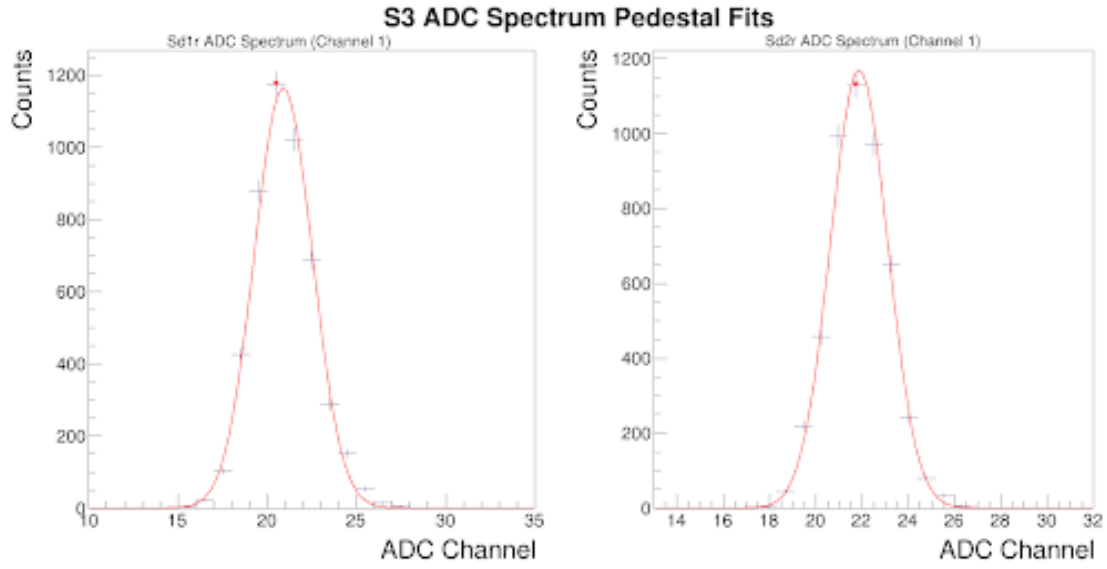

Figure 3.4: The pedestal ADC spectrum for the S3 detectors fitted with a gaussian.

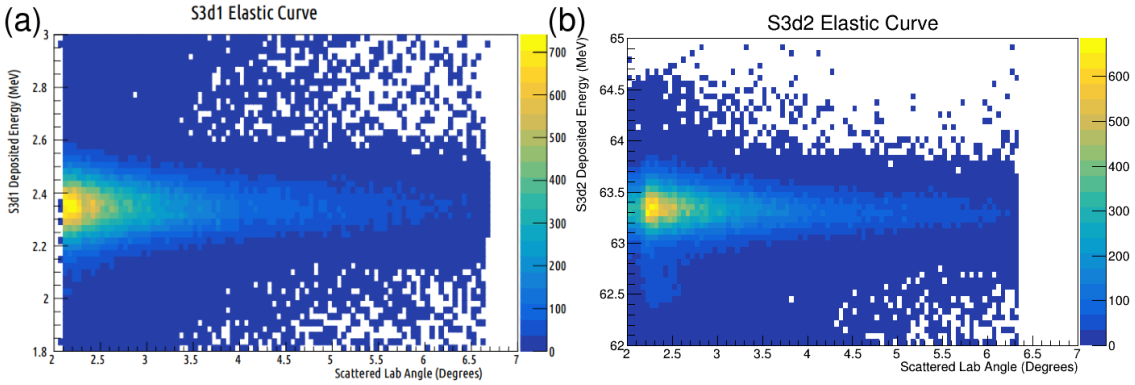

Figure 3.5: Calibrated energy vs. scattering angle for (a) S3d1 detector and (b) S3d2 detector

measure the thickness of the solid D_2 target.

3.4 TARGET THICKNESS MEASUREMENT

In this section, the method used to measure the thickness of the solid D_2 target will be discussed. As mentioned in the previous chapter, the D_2 target is sprayed on the Ag foil and then frozen, therefore the exact thickness of the target is not known.

The target thickness will be required to calibrate the CsI(TI) detector and generate the Q-value spectrum in the proceeding sections. To determine the target thickness the elastically scattered ^{8}He data from the S3 detectors with and without the solid D_2 target can be used. Stopping power calculations can be performed to determine the target thickness if the ^{8}He energy before and after the D_2 target is known. Let's define E_i as the energy of the scatter ^{8}He without the D_2 target and E_f as the energy with the D_2 target. The following relation can be used to find the target thickness,

$$t = \int_{E_i}^{E_f} \frac{1}{S(E)} dE \tag{3.4}$$

where $S(E)$ is the stopping power of the beam passing through the D_2 target given by Equation 3.1. E_i and E_f can be found by reconstructing the energy of the ^{8}He beam before it enters the S3 detectors. The ^{8}He charged particle will lose energy through the dead layers and the active silicon region of the S3d1 and S3d2 detectors. The energy lost in the active silicon is what the detectors measure. The energy of the ^{8}He particle entering the S3 detector can be reconstructed by back-tracing the particle's trajectory. Figure 3.6 shows the trajectory of a beam particle entering the S3 detectors. The energy of the beam entering the S3 detector can be reconstructed using the following,

$$E_{i/f} = E_{dl1} + E_{Sd1} + E_{dl2} + E_{Sd2} \tag{3.5}$$

where E_{dl1} and E_{dl2} are the energy losses through the dead-layers and E_{Sd1} and E_{Sd2} is the energy deposited in the active silicon regions. E_i is obtained from equation 3.5

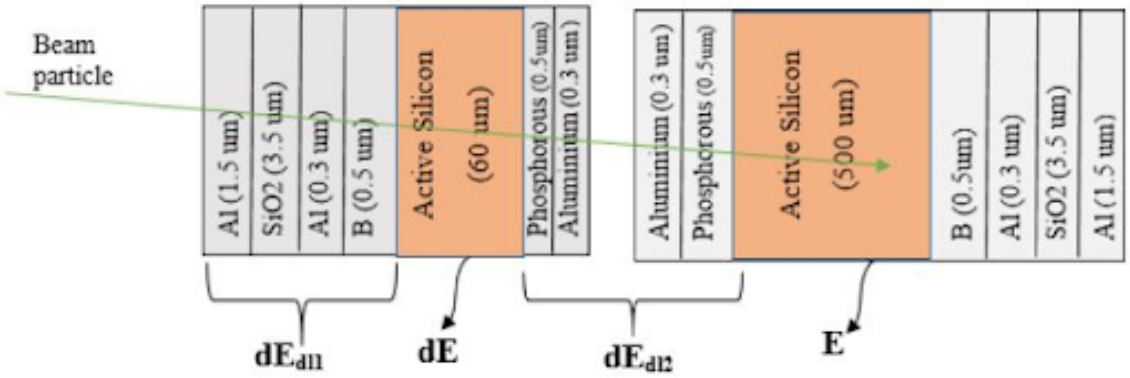

Figure 3.6: The trajectory of the scattered beam entering the S3 detector [3].

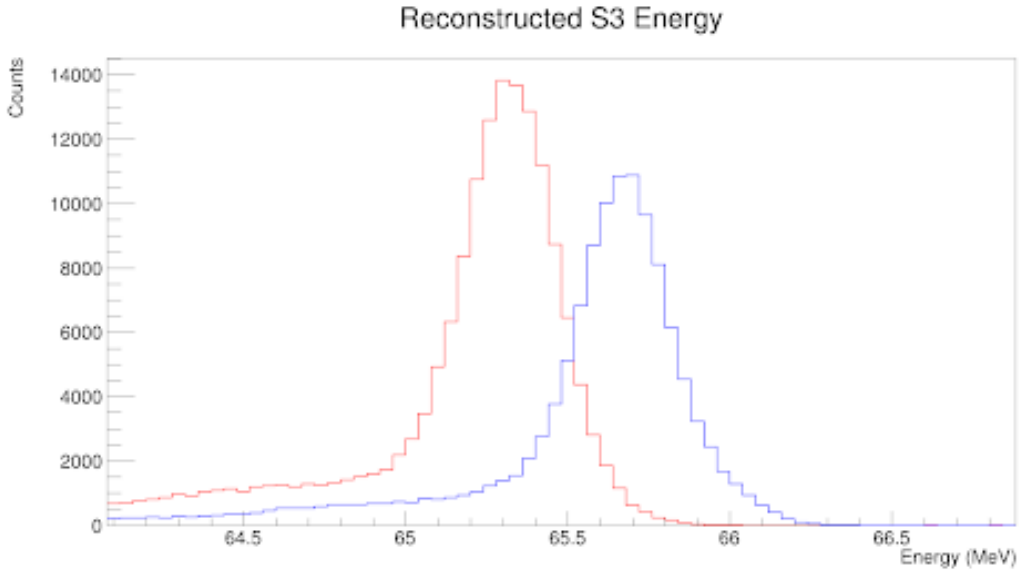

Figure 3.7: The reconstructed energy of the beam for a target run (red histogram) and a no-target run (blue histogram).

using data without the D_2 target present, while E_f is obtained from data with the D_2 target present. The reconstructed energies are shown in Figure 3.7. The mean values of the gaussians fitted to the peaks in Figure 3.7 are the energy of the scattered ^{8}He beam before and after the D_2 target i.e. E_i and E_f in Equation 3.4. The target thickness found throughout the experiment using Equation 3.4 is shown in Figure 3.8.

Initially, the measured target thickness was increasing abnormally as the experi-

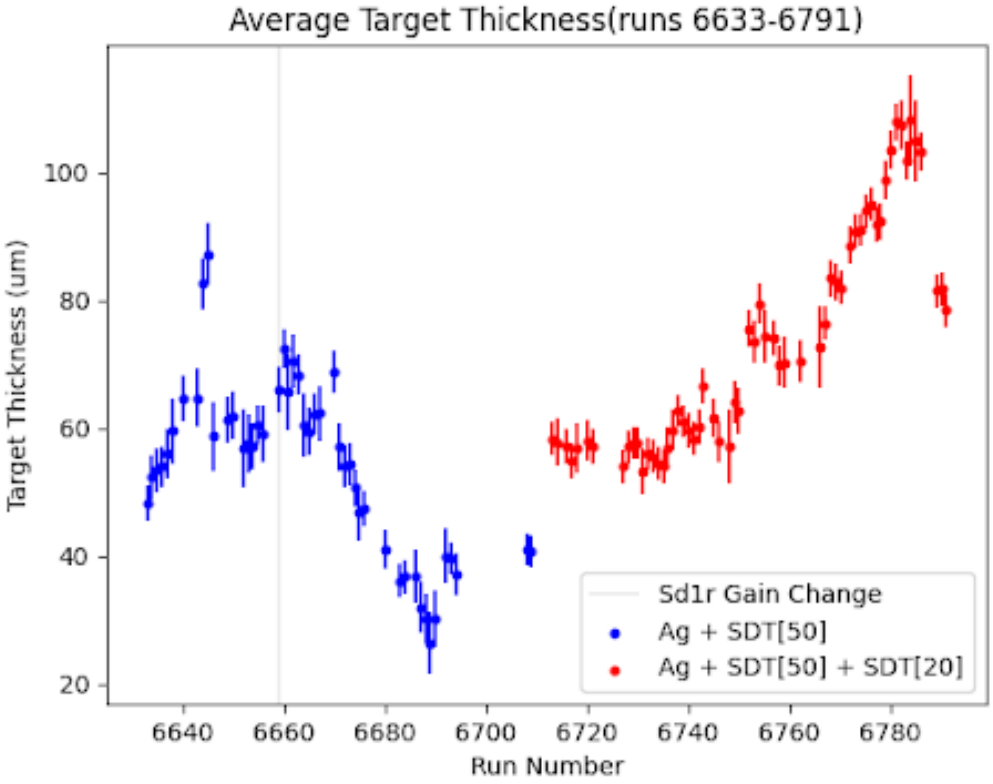

Figure 3.8: The measured target thickness throughout the experiment. The blue points are the originally formed target while the red point are the runs after additional D_2 gas was sprayed onto the target to account for evaporation. The target thickness was calculated with the corrected gain.

ment progressed. The gain in the S3d2 detector was found to shift over time. The issue was detected by tracking the peak position of the fixed pulse height peak generated by a pulser, the position of the pulser generated peak should remain constant. It was observed that the pulser peak position steadily declined as the experiment progressed and has a rapid drop near run 6800. This indicates that the gain is shifting and hence the gain parameters calculated in the previous section were required to be corrected to account for this gain drift. Figure 3.9 shows the position of the pulser peak throughout the experiment. This gain shift caused the reconstructed energy after the D_2 target to be incorrect and hence the wrong target thickness was measured. The gain was corrected using the following

$$g_c = g_b \frac{c_b - p_b}{c_c - p_c} \tag{3.6}$$

where g_c, p_c, c_c is the corrected gain, pedestal and pulser peak position of the current run respectively and g_b, p_b, c_b is the gain, pedestal and pulser peak position of a base run respectively. Figure 3.9 shows the corrected pulser peak position as well. With the gain correction, the target thickness was calculated based on runs 6640-6670 and 6713-6750 and found to be 60.1 $\mu m \pm$ 0.8 μm. Now that the thickness of the solid D_2 target is known, the CsI(TI) detector can be calibrated.

3.5 Downstream YY1 and CsI(TI)

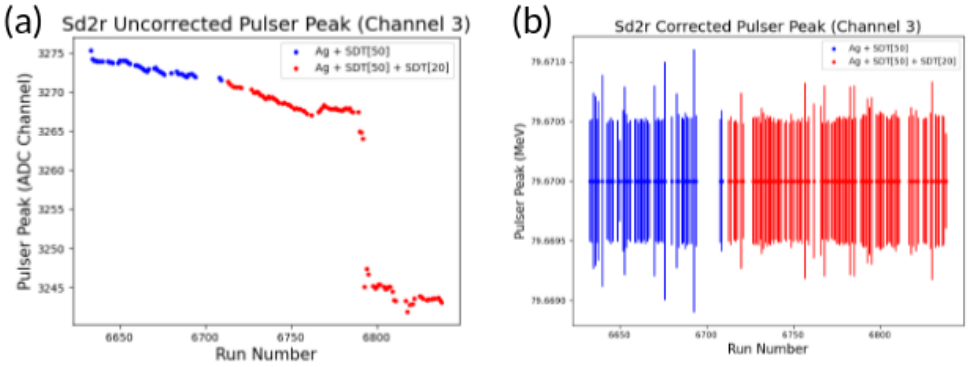

Figure 3.9: The peak position of the pulser generated peak for ring 3 of the S3d2 detector with the (a) original gains and (b) corrected gain.

3.5.1 YY1

The downstream YY1 detector was calibrated using a triple alpha source of ^{241}Am, ^{244}Cm, ^{239}Pu with peak energies of 5.15 MeV, 5.48 MeV, and 5.80 MeV respectively. The alpha particles emitted from the source deposited their energies in one of 128 YY1 segments. Figure 3.10 shows the uncalibrated energy of the alpha source in each detector channel. Figure 3.11 shows the ADC spectrum for a single segment of the YY1 detector. The plot in Figure 3.11 shows three peaks that correspond to the three peak alpha particles in the alpha source. These peaks were fitted with a gaussian and the mean value of the fitted gaussian was taken as the peak position. Since the energies of the alpha source and the peak positions are known, a least square fit was performed using equation 3.2 to find the gain and pedestal for each detector segment. Figure 3.12 shows the results of the fit i.e the calibrated YY1 spectrum is shown in Figure 3.12.

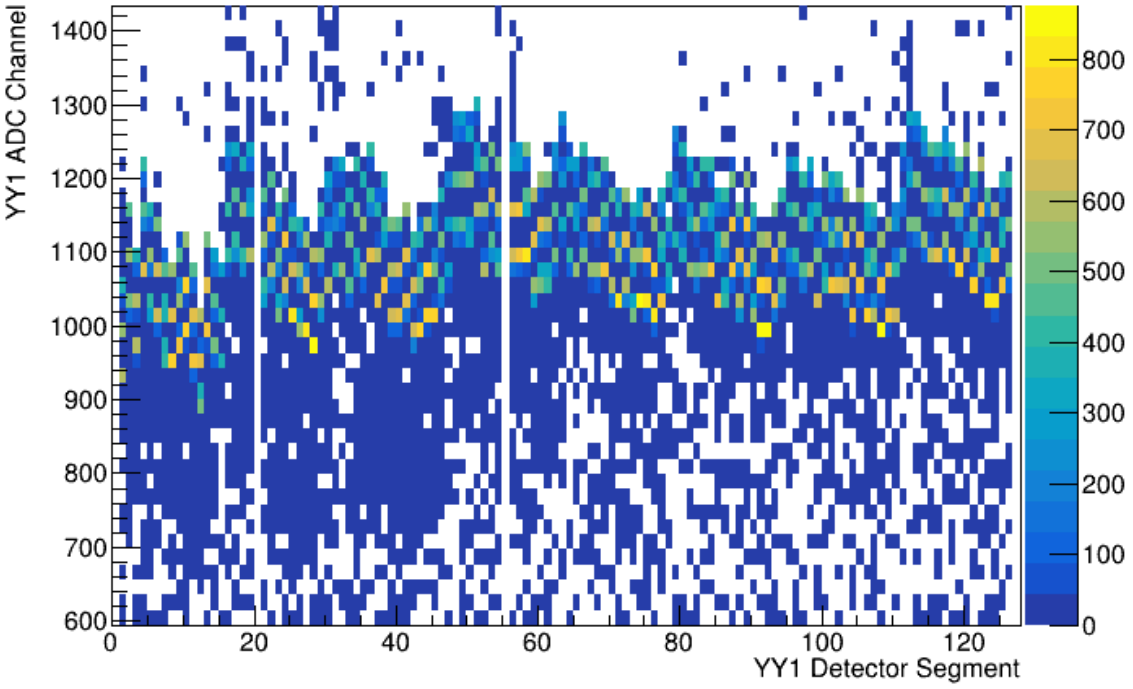

Figure 3.10: Uncalibrated YY1 detector ADC channel vs. YY1 segment

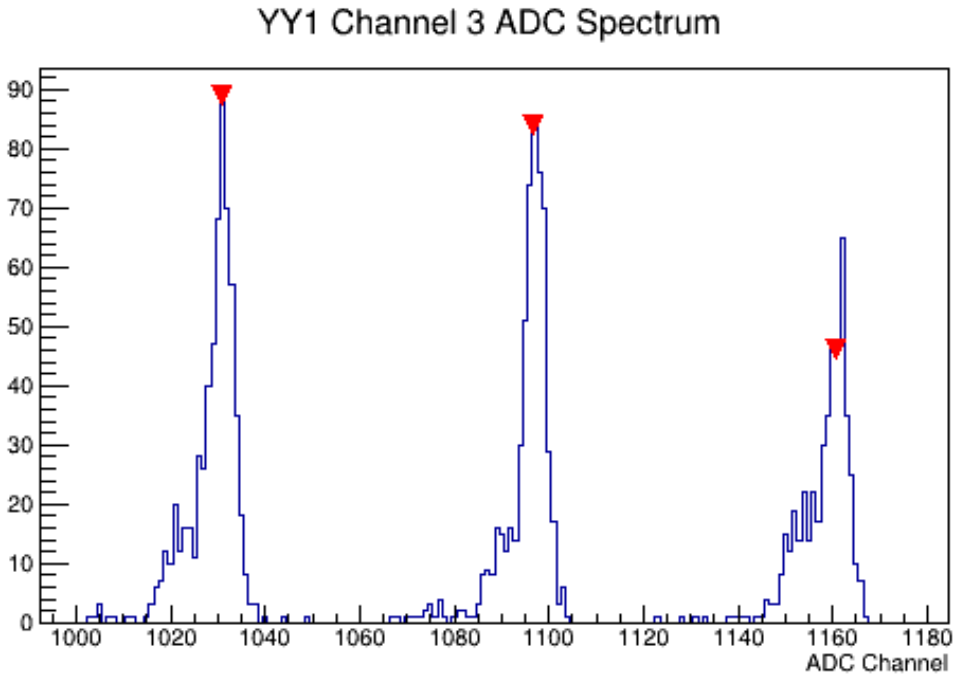

Figure 3.11: YY1 ADC spectrum for detector segment 3.

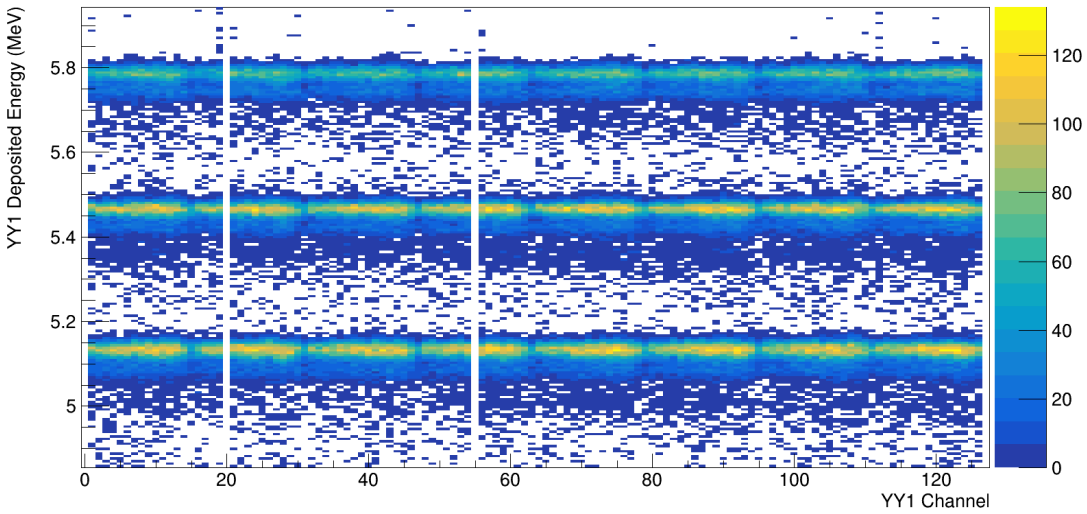

Figure 3.12: Calibrated YY1 energy vs. YY1 segment

3.5.2 CsI(TI)

The CsI(TI) detector could not be calibrated with an alpha source so the elastically scattered deuterons from the target were used. The first step is to select the deuteron events. As discussed in Chapter 2 the YY1 and CsI(TI) detectors create a ΔE-E telescope that can be used to identify light particles. Figure 3.13 shows the energy deposited in the YY1 detector versus energy deposited in CsI(TI). The red polygon is the deuteron events. Next, the elastically scattered deuterons must be selected and this can be done by looking at events within the elastic curve. Figure 3.14 shows the CsI(TI) ADC channel vs. scattered laboratory angle of the incident particle. The red polygon is the selected elastically scattered deuterons.

Now that the elastic deuterons are selected, the energy they would deposit in the CsI(TI) needs to be calculated. This can be done by calculating the energy lost by the beam through the IC to the point of scattering. The scattering event will occur

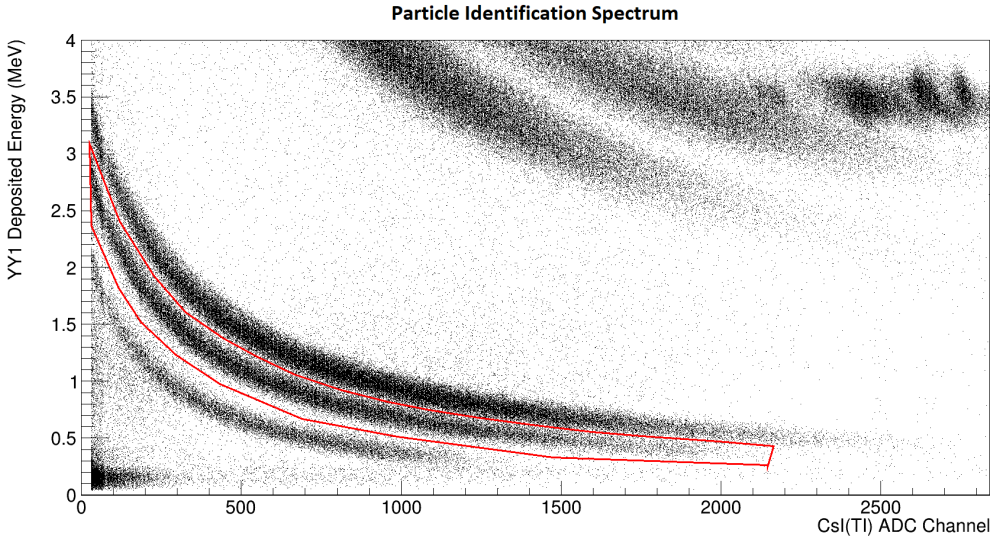

Figure 3.13: The particle identification spectrum for light particles. The red polygon is the deuteron events.

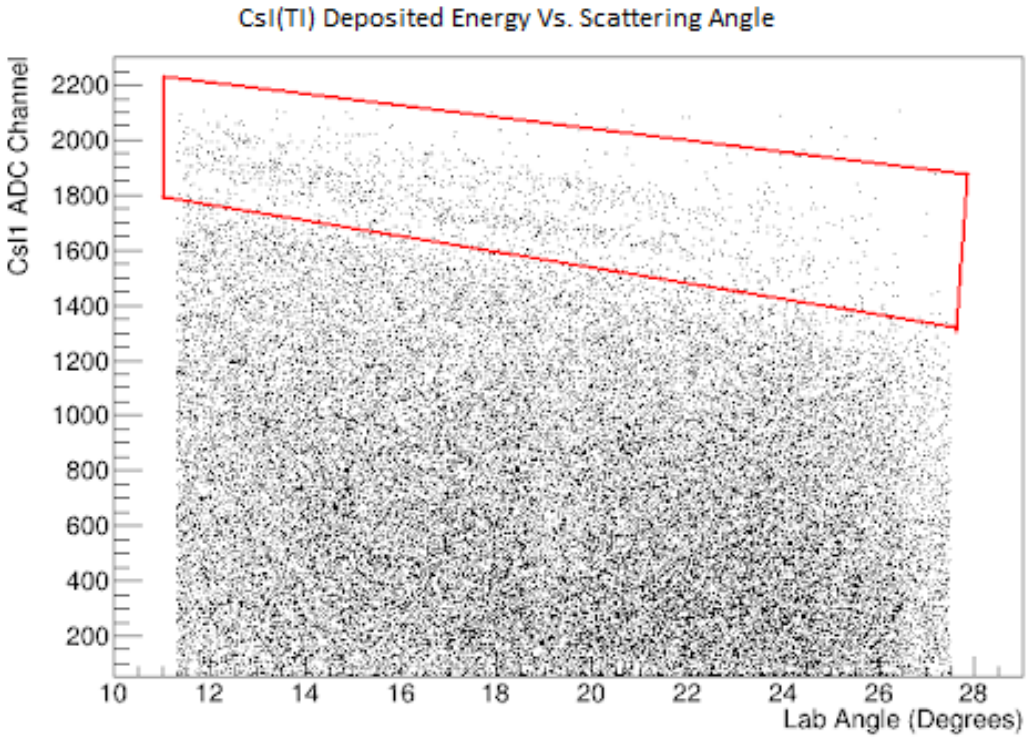

Figure 3.14: The ADC channel vs. laboratory angle for the scattered deuterons incident on CsI(TI) detector. The red polygon are the elastically scattered deuterons.

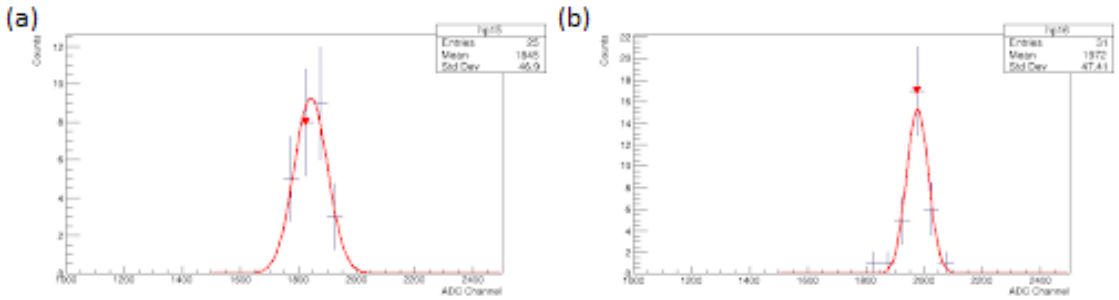

Figure 3.15: The ADC spectrum fits for sector 5 of the CsI(TI) detector for (a) the first angular region and (b) the second angular region.

at a random point within the D_2 target but on average the scattering will occur in the middle of the target. After the deuteron scattered the energy loss through the YY1 dead-layers/active silicon region and the CsI(TI) dead-layers were taken into account.

The energy deposited in the CsI(TI) detector is dependent on the incident angle of the particle so this needs to be taken into account when calibrating. The angular dependence is dealt with by gating events correlated to a specific angular segment of the YY1 detector. Due to low statistics for individual segments, it was decided that the calibration will be done on groups of four angular segments. The ADC spectrum for each CsI(TI) sector was fitted with a gaussian for each angular segment. Figure 3.15 shows the raw ADC spectrum and fits for two angular segments for a specific CsI(TI) sector. The pedestals can be found by finding the peak position in the ADC spectrum with a gaussian for each detector segment using a pedestal run. Finally, Equation 3.3 can be used to find the gain for each CsI(TI) sector for all four angular segments.

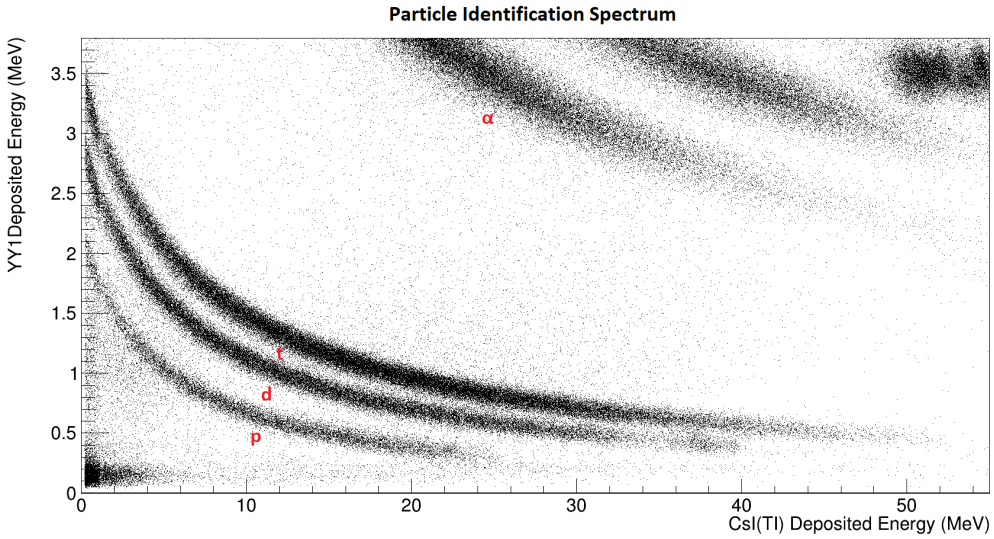

Figure 3.16: The calibrated particle identification spectrum for light particles.

3.6 PARTICLE IDENTIFICATION

As mentioned previously the YY1 and CsI(TI) detectors create a ΔE-E telescope which can be used to identify light nuclei picked up by the detectors. This is done since most particles will not stop and only lose some of their energy in the YY1 detector depositing the rest of their energy in the CsI(TI) detector. From equation 3.1 the energy the particle loses in the YY1 detector is proportional to Z^2 and the remaining kinetic energy is deposited into CsI(TI) which therefore is related to the mass number, A. The latter allows for particles with a common atomic number to be differentiated by mass. Figure 3.16 shows the ΔE-E plot and the identified particles which includes protons (p), deuterons (d), tritons (t), and alpha particles (α).

3.7 Derivation of Q-Value Spectra

The Q-value is defined as the difference in the total mass before and after the reaction. Therefore the measured Q-value spectrum can give us useful information on the scattered particles. Given a reaction of the following form,

$$A + b \rightarrow C + d \tag{3.7}$$

the Q-value in natural units ($c = 1$) is given by the following expression,

$$Q = m_A + m_b - m_C - m_d \tag{3.8}$$

where m_A,m_b, m_C, m_d is the rest masses of the particles. From equation 3.8 you would expect the Q-value for an elastic scattering reaction to be zero as $m_A = m_C$ and $m_b = m_d$. In the reaction of interest ^{8}He(d,d)^{8}He, there is a possibility that ^{8}He will enter an excited state, and hence m_C will be different from the rest mass by the mass-energy equivalents. Equation 3.8 can be modified as follows,

$$Q = m_A + m_b - m_d - \sqrt{E_C^2 - P_C^2} \tag{3.9}$$

where E_C^2 and P_C^2 are kinetic energy and momentum of the scattered ^{8}He respectively. E_C^2 and P_C^2 can be found in terms of quantities that are known or can be measured as follows,

$$E_C = E_A + m_A + m_b - E_d - m_d \tag{3.10}$$

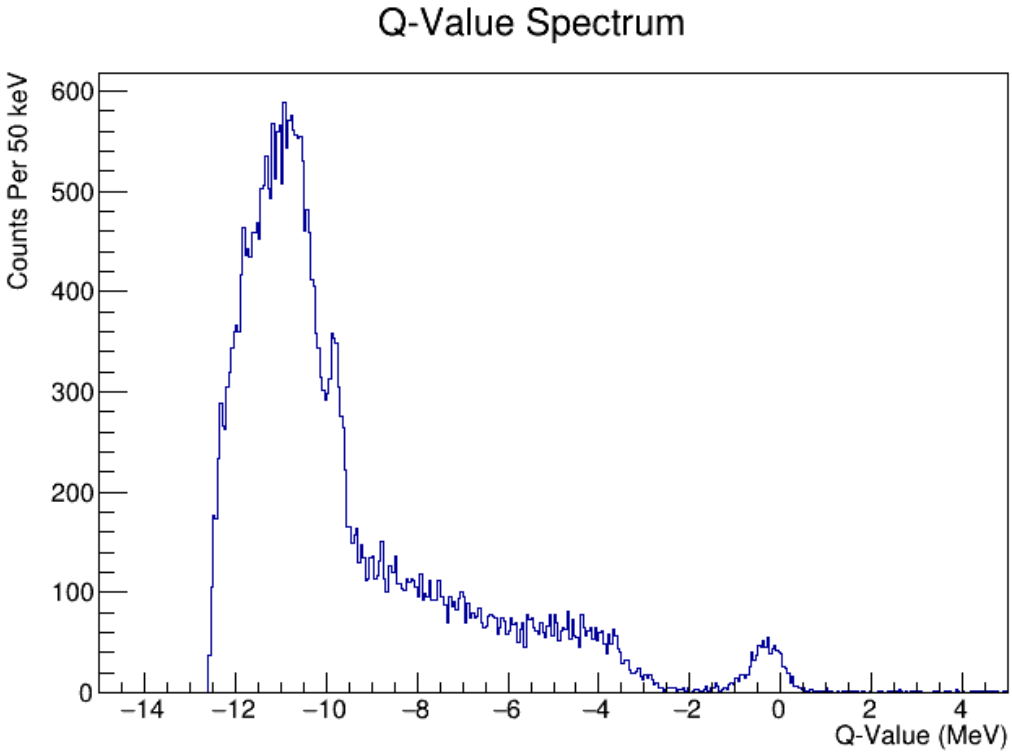

Figure 3.17: The Q-value spectrum generated using the missing mass technique.

$$P_C = \sqrt{P_A^2 + P_d^2 - 2P_A P_d cos\theta_d} \tag{3.11}$$

where E_A is the energy of the RIB midway through the solid deuterium target, P_A and P_d is the momentum of the products, E_d and θ_d are the kinetic energy and scattering angle of particle d respectively. P_d, E_d, and θ_d can be measured from the data while the rest are known quantities. Figure 3.17 shows the generated Q-value spectrum. The spectrum to the left of -2 MeV in the Q-value spectrum is the non-elastic spectrum i.e. the portion of the Q-value spectrum from the inelastic scattering reaction. The spectrum to the right of -2 MeV is the elastic spectrum which is the portion of the Q-value spectrum from the elastic scattering reaction.

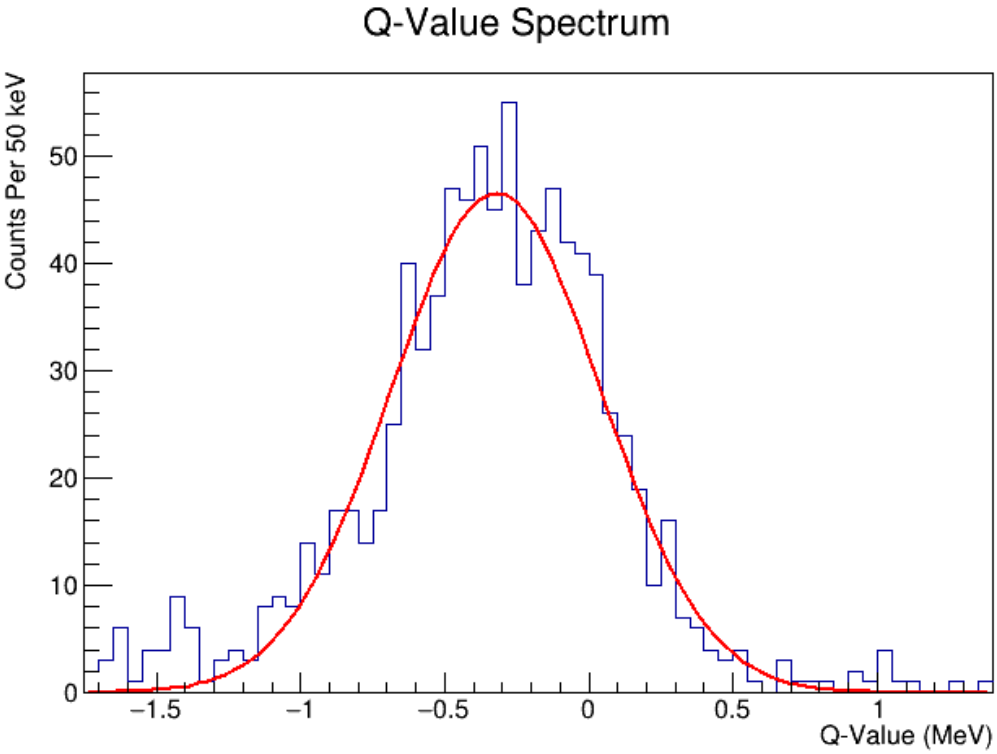

Figure 3.18: The ground-state peak fitted with a gaussian.

The excitation spectrum can be found from the Q-value with the following,

$$E_{excited} = Q_{g.s} - Q \tag{3.12}$$

where $Q_{g.s}$ is the Q-value of the ground state. The ground state peak in the Q-value spectrum was fitted with a gaussian to find its peak position. Figure 3.18 shows the ground-state peak. The ground state was observed to be at -0.33 ± 0.01 MeV. This means that there is a -0.33 MeV shift in the Q-value spectrum since the ground state is expected to be observed at 0 MeV. The possible reasons for this shift will be discussed further in the next chapter.

Chapter 4

Discussion

The Q-value spectrum for ^{8}He was measured with data collected at IRIS through scattering reactions. The observed Q-value spectrum shown in Figure 3.17 shows the ground state peak to be located at -0.33 $\pm$ 0.01 MeV. This means that there is approximately a -0.33 MeV shift in the Q-value spectrum since the expected position of the ground-state peak is 0 MeV. One possible reason for this shift could be due to uncertainty in the CsI(TI) calibration parameters. The CsI(TI) detector, even with taking bins of four angular segments, had a low number of statistics. To check if the low statistics caused any issues with the determined calibration parameters, one could check to see if the measured elastic curve for the deuterons agreed with simulations or not. Depending on the results of the simulations a different approach for calibrating the CsI(TI) detector may need to be taken.

A second issue in the observed data is with the target thickness. In Figure 3.8 even after the gain correction was employed there is still a rapid increase in target thickness from runs 6760 onwards that has yet to be explained. Further employing the gain correction on runs after 6800 results in non-physical target thicknesses. A possible reason for this could be that a change in the beam energy could have occurred. Another explanation could be that along with the shift in gain there could have also been a shift in the pedestal. This unresolved issue with target thickness could have

also contributed to the shift in the Q-value spectrum that was observed.

Whether a low-lying SDM is present in ^{8}He's excitation spectrum is still undetermined. Additional data analysis needs to be performed to resolve the issues with the Q-value spectrum to get an accurate measurement of the excited states of ^{8}He. Once the excitation spectrum gets generated the next steps would be to simulate non-resonant background reaction channels. After subtracting all background channels, if resonance peak(s) is/are observed their angular distribution will be determined to see if a SDM is observed.

Bibliography

[1] URL: http://www.micronsemiconductor.co.uk/yy1/.

[2] URL: http://www.micronsemiconductor.co.uk/s3/.

[3] URL: https://iris.wiki.triumf.ca/wiki/S3.

[4] M.S. Golovkov et al. "The 8He and 10He spectra studied in the (t,p) reaction". In: *Physics Letters B* 672.1 (2009), pp. 22–29. ISSN: 0370-2693. DOI: https://doi.org/10.1016/j.physletb.2008.12.052. URL: https://www.sciencedirect.com/science/article/pii/S0370269308015608.

[5] L. Grigorenko et al. "Soft Dipole Mode in ^{8}He". In: *Physics of Particles and Nuclei Letters* 6 (Mar. 2009), pp. 118–125. DOI: 10.1134/S1547477109020046.

[6] M. Holl et al. "Proton inelastic scattering reveals deformation in 8He". In: *Physics Letters B* 822 (2021), p. 136710. ISSN: 0370-2693. DOI: https://doi.org/10.1016/j.physletb.2021.136710. URL: https://www.sciencedirect.com/science/article/pii/S037026932100650X.

[7] R. Kanungo. "IRIS: The ISAC charged particle reaction spectroscopy facility for reaccelerated high-energy ISOL beams". In: *Hyperfine Interactions* 225 (1 2014), pp. 235–240. DOI: 10.1007/s10751-013-0904-8.

[8] R. Kanungo et al. "Evidence of Soft Dipole Resonance in ^{11}Li with Isoscalar Character". In: *Phys. Rev. Lett.* 114 (19 May 2015), p. 192502. DOI: 10.1103/PhysRevLett.114.192502. URL: https://link.aps.org/doi/10.1103/PhysRevLett.114.192502.

[9] Kenneth S Krane. *Introductory nuclear physics*. New York, NY: Wiley, 1988. URL: https://cds.cern.ch/record/359790.

[10] Karin Markenroth Bloch et al. "8He-6He: A comparative study of nuclear fragmentation reactions". In: *Nuclear Physics A* 700 (Mar. 2002), 3–16. 1.525 Impsct Factor. DOI: 10.1016/S0375-9474(00)00372-9.

[11] Steven C. Pieper, R. B. Wiringa, and J. Carlson. "Quantum Monte Carlo calculations of excited states in $A = 6 - 8$ nuclei". In: *Phys. Rev. C* 70 (5 Nov. 2004), p. 054325. DOI: 10.1103/PhysRevC.70.054325. URL: https://link.aps.org/doi/10.1103/PhysRevC.70.054325.

[12] *The Colorful Nuclide Chart*. URL: https://people.physics.anu.edu.au/~ecs103/chart/.

[13] J. Xiao et al. "New measurements for 8 He excited states". In: *Chinese Physics Letters* 29 (2012), p. 082501.